

Seismic velocity and attribute study based on well interpolated data

Douglas Gratwick and Daniel Rosales¹

ABSTRACT

This paper studies the effects of fluid type in pore space for a channel sand in the Stanford V dataset. The model used was created by interpolation of 3D well data using ordinary kriging. V_p , V_s , density, and porosity were all kriged into 3D volumes, and then a slice was extracted, which contained a sand body surrounded by a shale. Elastic modeling was run on this slice, and the data were processed into CMP gathers for AVO study. Subsequent modeling was done for fluid substitution of both oil and gas. It was found that the hydrocarbons yielded higher amplitude reflections, and that the gas model showed an increased amplitude with offset. A velocity slice containing well information was used for modeling and subsequent velocity analysis. This velocity analysis shows the difference between seismic and well velocities due to the frequency content of the source.

INTRODUCTION

Seismic data can provide not only structural information but also rock property information like P and S velocity, porosity, fluid saturation, etc. Amplitude corresponds to the dynamic feature of seismic data and its behavior with respect to incidence angle (AVA) or offset gives information about both the fluid type and fluid saturation in the rock (Ostrander, 1984; Chen and Sidney, 1997).

Velocity, another rock property, is a key factor not only for the rock property estimation but also for the final image in the seismic processing step. Different sources of velocity information (well data, seismic data) yield different velocity values, partly because of the frequency dependence of this rock property (scale effect). A connection between the different velocity values is a key factor for reservoir characterization studies.

This paper presents a study of the effect of pore fluid type on seismic data, and an analysis of the differences between seismic and well velocities. This study is based on the information of well data only; in order to achieve our goal, a three dimensional interpolation of the well data is required.

Geostatistics is a field which has many algorithms for handling the 3D interpolation problem. Kriging is a technique which is very useful, especially when dealing with sparsely sam-

¹email: doug@sep.stanford.edu daniel@sep.stanford.edu

pled data, such as wells in 3D. In this project, an ordinary kriging operator is applied to the well data (White, 1998).

This work intends to give not only relations between pore fluids and seismic data but also compares well velocities and seismic velocities based on well data interpolation and 2D seismic modeling. The use of *Gassmann's equation* for fluid substitution (brine→oil, brine→gas) will help to study the fluid saturation effects. Seismic modeling over the sections after and before fluid substitution shows *AVO* differences due to the pore fluid. A second seismic modeling is done for velocity analysis purposes, this velocity analysis presents differences between seismic and well velocities.

WELL INTERPOLATION

The data for this project was supplied by the rock physics group at Stanford University. It is from the Stanford V synthetic data set, which is a 3-D model set in a fluvial environment. The trajectories for the wells used in this project are displayed in Figure 2. The geometry represents wells from three separate platforms. In order to extract inline slices easier, the data was rotated 37° to an inline azimuth of 0° or directly north south, as shown in Figure 1.

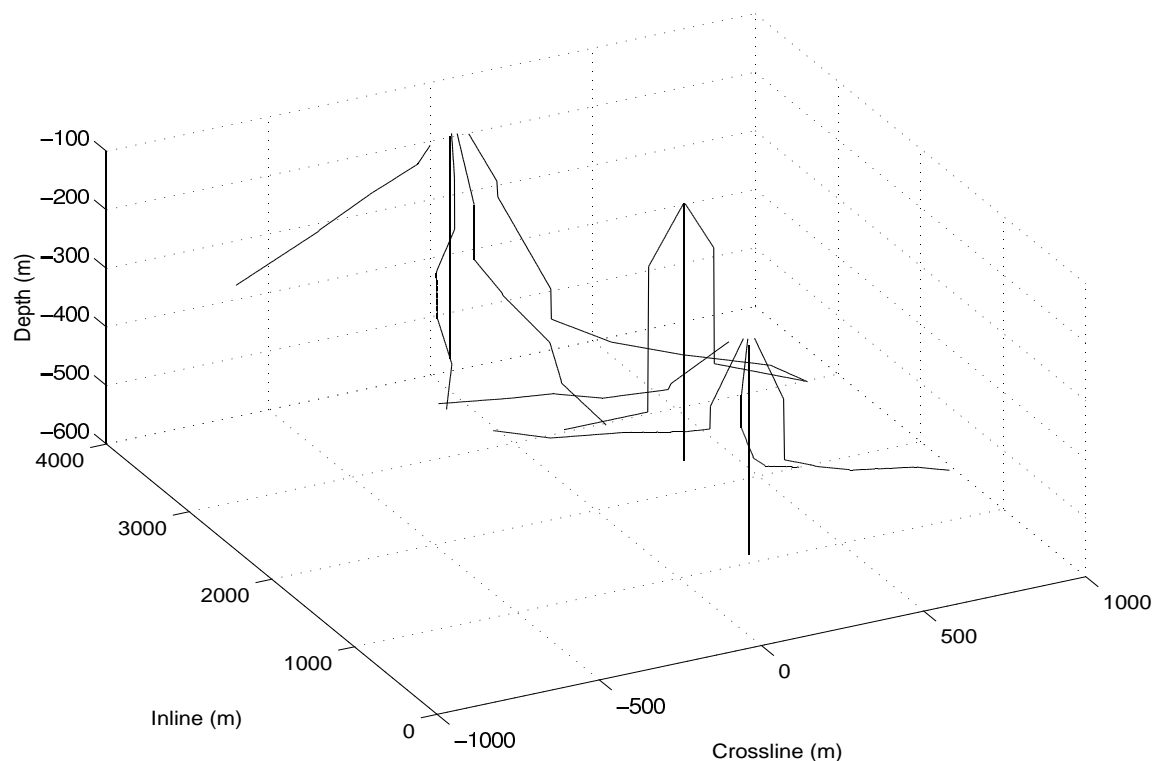


Figure 1: Rotated wells to N-S axis. `daniel1-rotated_wells` [NR]

The interpolation between the wells was done using an ordinary kriging method. The actual operator is a part of the `kt3d` program in the *GSLIB* software package (Deutsch and

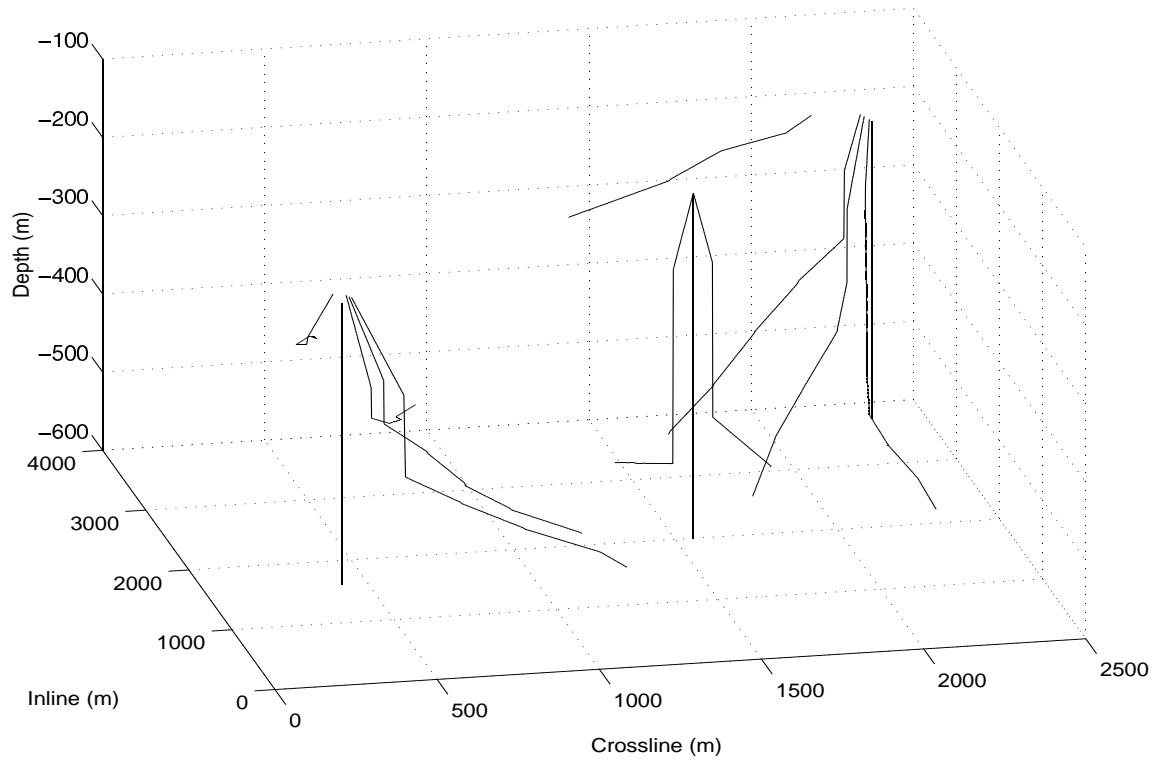


Figure 2: Original orientation of well data. daniel1-wells [NR]

Journal, 1998). The distance dependence of the kriging operator is found by looking at variograms. Variograms were calculated using the program `gamv`, another part of the *GSLIB* library. The horizontal variogram, Figure 3, shows better correlation at greater distances than the vertical variogram, Figure 4. This is expected because in a real geologic setting, rocks usually are deposited in roughly horizontal packages which usually are much wider than they are deep. The actual variogram was a semivariogram, which is commonly used to correlate two attribute values separated by a distance vector,

$$\gamma(\vec{h}) = \frac{1}{2N(\vec{h})} \sum_{i=1}^{N(\vec{h})} (x_i - y_i)^2, \quad (1)$$

where $N(\vec{h})$ is the number of attribute pairs, x_i is the start or *head* value, and y_i is the end or *tail* (Deutsch and Journel, 1998). Thus, typically the value γ will be zero where a data point is, and increase sharply then flatten off at great distances where there is no correlation between the head and tail points. The data fitting lines are exponential fits, which were fit in the equation:

$$\gamma(\vec{h}) = c \cdot \left[1 - e^{-\frac{3h}{a}} \right], \quad (2)$$

where a and c are found using a non-linear least squares algorithm. These values are used in the *kt3d* program. The ordinary kriging program uses the kriging estimator in the following

equation (Journel, 2000),

$$Z_{OK}(\vec{u}) = \sum_{\alpha=1}^n \lambda_{\alpha}^{(OK)}(\vec{u}) Z(\vec{u}_{\alpha}). \quad (3)$$

Basically, the ordinary kriging operator estimates at each location \vec{u} a mean. The variance specified in the program is the same everywhere, and is defined in the program using a and c from equation (3). The ability to re-estimate the mean at each point is what differs ordinary kriging from simple kriging. This ability makes the ordinary kriging a robust technique because the random function model can be rescaled at each point. The robustness makes ordinary kriging appropriate for this problem, since the data is sampled so sparsely. This brief discussion of variograms and ordinary kriging is based on the discussion in the software users guide (Deutsch and Journel, 1998).

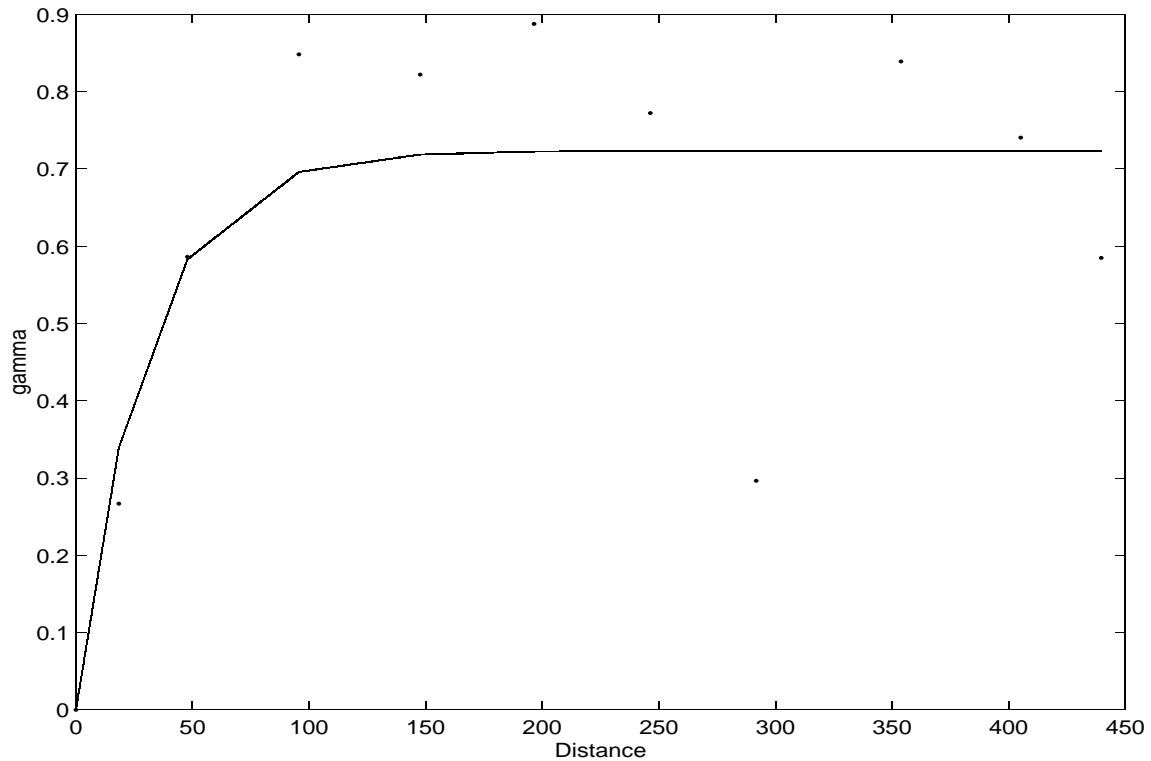


Figure 3: Horizontal variogram. `daniel1-hoz_var` [NR]

Figure 5 shows the 2D velocity slices used for the *AVO modeling* and *velocity modeling*. The slices correspond to the 0 m and 300 m crossline value in Figure 1, respectively. In these slices the data are the most dense, and thus the kriging algorithm is the most accurate. The slices from the output was 30 points on the depth axis, and 160 points on the distance axis. This was too coarse for the modeling, so a linear interpolation program was used to make the model 300 by 2000 points.

The lateral velocity distribution around the well location in Figure 5b demonstrate the stability of the interpolation operator because of the gradual lateral decay of the velocities and the

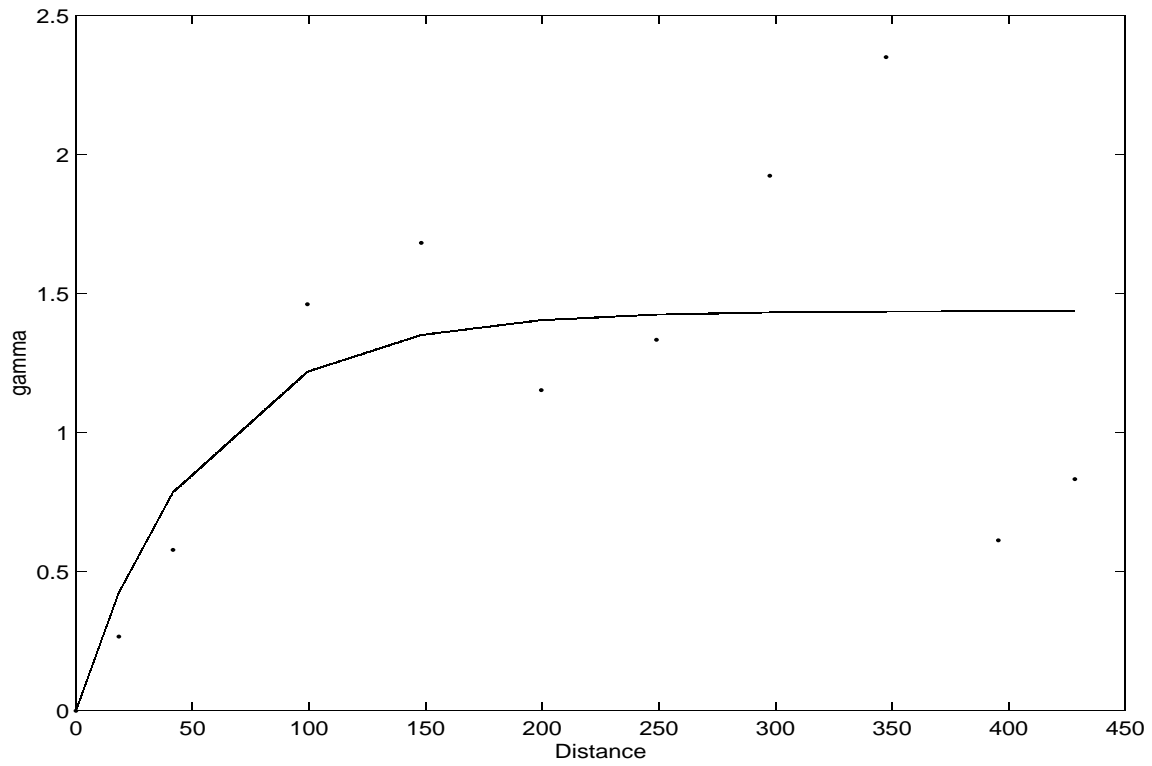


Figure 4: Vertical variogram. `daniel1-vert_var` [NR]

a

b

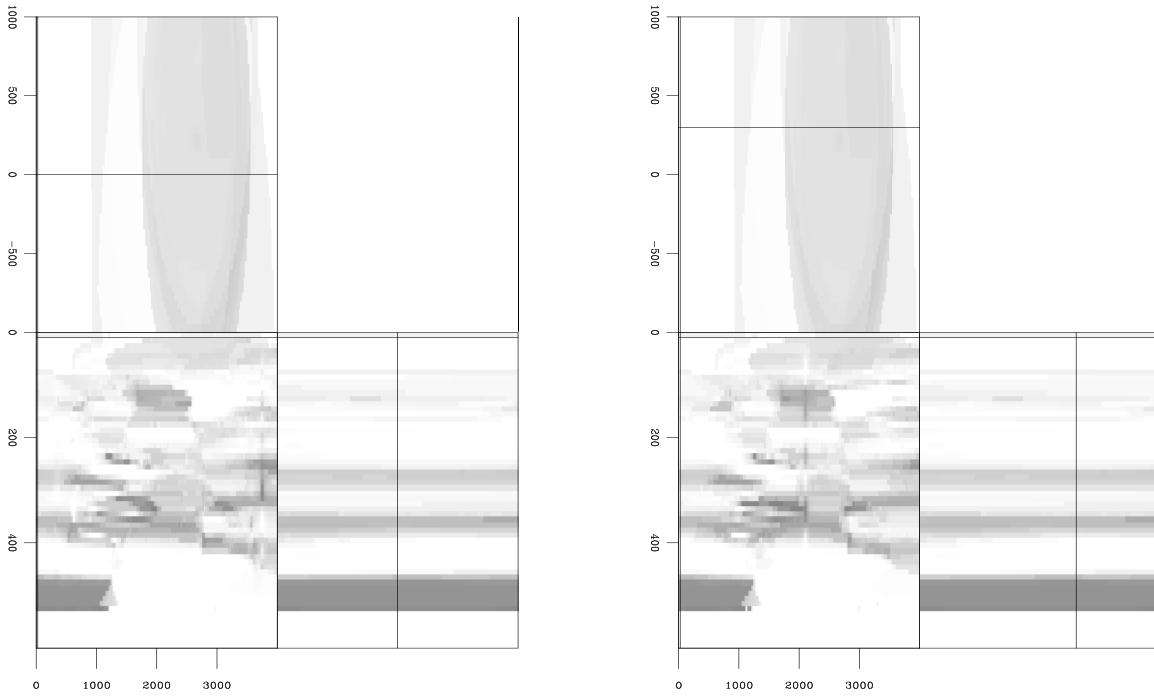


Figure 5: Slices from 3-D data cube used in the modeling. `daniel1-slice` [ER]

absence of either vertical or horizontal fluctuations of the velocity distribution. It is not possible to assess the accuracy of the interpolation process because we do not have the original velocity model; however, the fact that it is possible to distinguish some bodies with lense shapes, which is a geological reasonable distribution of fluvial sedimentary environment, makes the model seem reasonable.

FLUID SUBSTITUTION

In order to study the effects of different fluids on AVO response, a suitable body in the diagram needed to be located which would show significant rock property change with a change in fluid (Mavko and Mukerji, 1995). Specifically, a body with high porosity would be the best choice. In Figure 5a there is a prominent feature in the center of the section at a depth of 100 meters, a thickness of 50 meters, and a width of around a kilometer. This body is interpreted as one of the many channel deposits present within the Stanford V dataset. The facies of this body is a relatively porous sand, with an associated low density, P-wave velocity, and S-wave velocity. The wide lateral extent, horizontal boundary, and sharp impedance contrast at both the top and base provide for good modeling because data can be looked at over a range of horizontal distance, and the amplitudes should be relatively strong (Yilmaz, 1987).

The inputs needed to do the fluid substitution are the P-wave velocity, S-wave velocity, density, and porosity. Since the kriging uses spatial coordinates, and each of these variables is known at well locations, the same kriging parameters are used for the other variables as was used for the P-wave velocity kriging. This ensures that the rock properties of the sand body are relative throughout. S-wave velocities were given for only one horizontal well. Since S-wave velocities were needed in the whole section equation (4) was used to calculate V_s from V_p using knowledge of facies.

The facies in the Stanford V dataset are ranked from 0-3, with lower numbers associated with slower, more porous facies. Using knowledge of the facies at each point, and the Castagna relation,

$$V_s = a_{i_2} V_p^2 + a_{i_1} V_p + a_{i_0}, \quad (4)$$

with the correct coefficients a_{i_2} , a_{i_1} , and a_{i_0} (refer to Appendix), a value for V_s was assigned to each point (Mavko, 2000). So on each variable section, including V_s , the sand body is a very prominent feature. From the porosity section in Figure 7, it is seen that in fact there is a high porosity anomaly associated with this channel sand. The original data is assumed to be saturated with a brine fluid. Values for V_p , V_s , and density of the brine saturated section (original data) are seen in Figure 6. Because this body is different than the surrounding rocks, the fluid substitution is easily implemented by simple scanning for anomalously low P-wave velocities in that area, and doing the fluid substitution at these points. The substitution requires units of K, bulk modulus, and μ shear modulus. Conversion using the kriged sections requires a calculation at each point,

$$K_{sat} = \rho \left(V_p^2 - \frac{4}{3} V_s^2 \right) \quad (5)$$

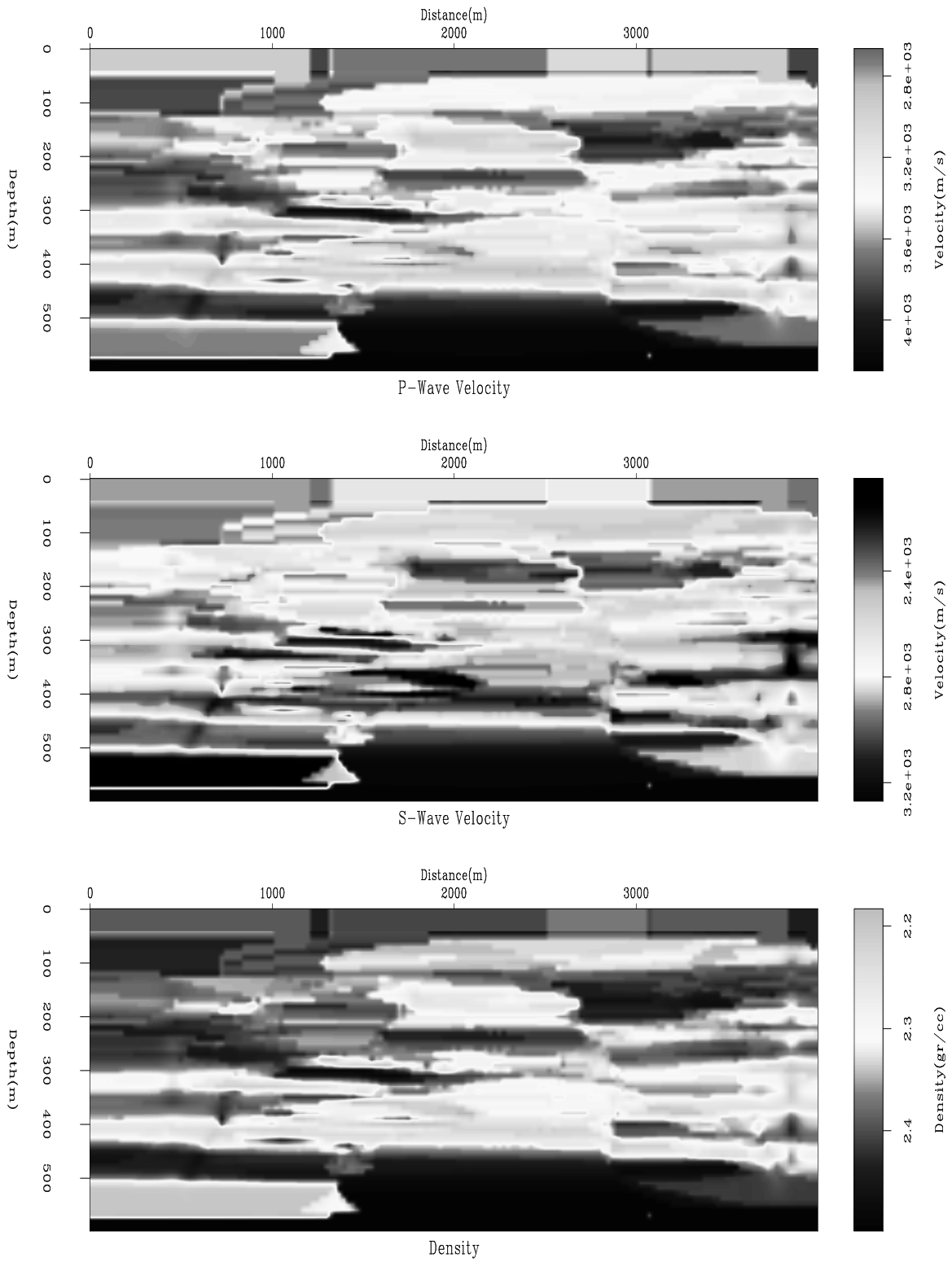


Figure 6: Brine-saturated section. `daniell-brine_plot` [ER]

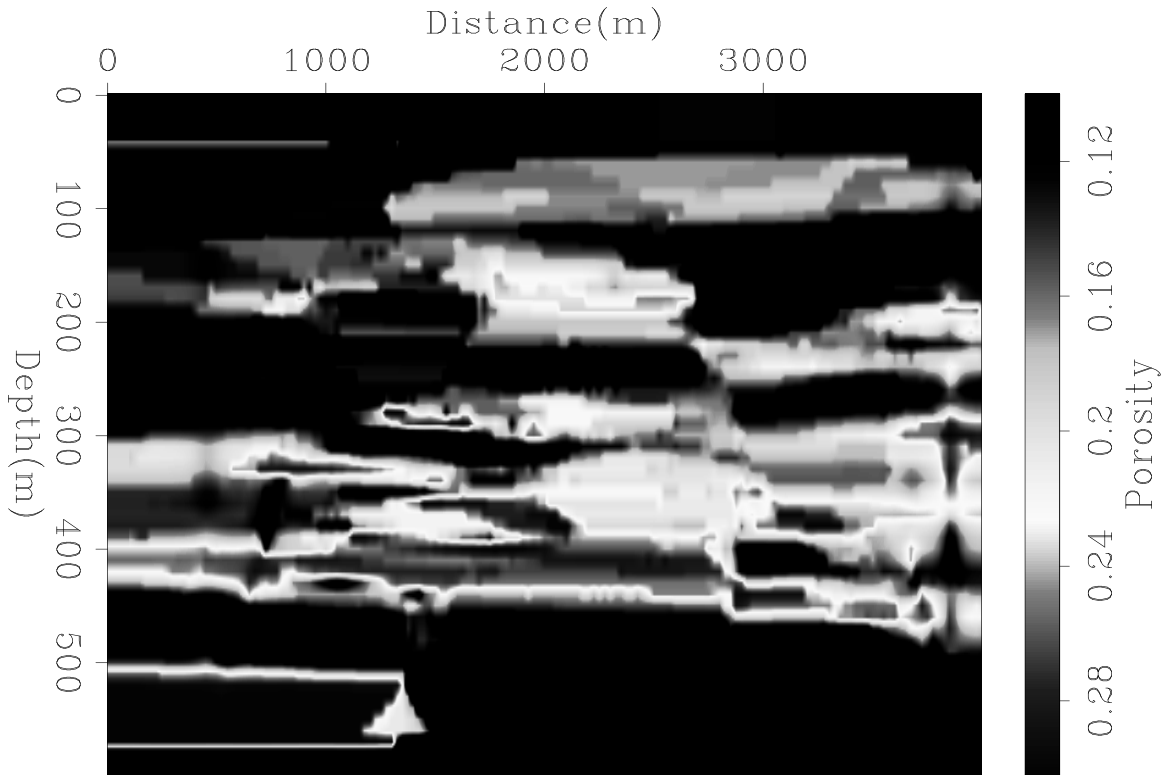


Figure 7: Porosity section. daniel1-por [ER]

$$\mu_{sat} = \rho V_s^2. \quad (6)$$

The substitution is done using the Gassmann's Relations obtained from Mavko (2000) (Equations 5 and 6). One Gassmann assumption is that the shear modulus, μ , is the same for a dry and fluid saturated rocks. This is a safe assumption since μ for fluids and gases is zero. The transform from brine saturated to dry is as follows:

$$K_{dry} = \frac{K_{sat} \left[\frac{\phi K_{min}}{K_{fluid}} + 1 - \phi \right] - K_{min}}{\frac{\phi K_{min}}{K_{fluid}} + \frac{K_{sat}}{K_{min}} - 1 - \phi} \quad (7)$$

where K is the Bulk modulus ϕ is the porosity. The mineral is assumed to be quartz, with $K=36.6$ Gpa. With this K_{dry} , the K_{sat} for and fluid can be found using the following relation:

$$K_{sat} = K_{dry} + \frac{\left[1 - \frac{K_{dry}}{K_{min}} \right]^2}{\frac{\phi}{K_{fluid}} + \frac{1-\phi}{K_{min}} - \frac{K_{dry}}{K_{min}^2}} \quad (8)$$

where the K_{min} is again assumed to be 36.6 Gpa for quartz (Mavko, 2000). Using this algorithm, the sand body was substituted with both oil ($K=0.5$ Gpa, $\rho=0.6$ g/cm³) and gas ($K=0.03$ Gpa, $\rho=.116$ g/cm³). The plots of V_p , V_s , and density are shown in Figure 8 and Figure 9 for

oil and gas substitution, respectively. As expected, the substitution of oil and gas decrease V_p because these fluids are not as stiff as brine. The densities go down as well, and this causes an increase in V_s , because μ stays the same.

MODELING

Two data sets were modeled in this paper. One data set was used for the AVO analysis and the other for the velocity analysis. Both modeling were done using the velocity interpolation result, and the main difference in both models is the velocity slice used. The AVO model was done over one velocity slice with a good definition of the sand lens for fluid substitution purpose. The velocity analysis model was done over another velocity slice containing one well in order to make the comparison of seismic and well velocities.

A synthetic modeling program, which solves the 2D elastic wave equation by explicit finite difference 2nd order in time and 16th order in x and z , was used for the modeling of the two data sets presented here. Both models consisted of 60 shots and 100 receivers per shot, with an spacing of 2 m between shots and receivers. The maximum two-way travel time was 0.1750 sec.

Since the sand body selected for the AVO study has a width of 50 m, with an average velocity of 2700 m/s, A wavelet with a wavelength less than 50 m is necessarily in order to have a good resolution of top and bottom of our target, because of this a *Ricker* zero-phase wavelet with a maximum frequency of 500 hz was used for both modeling, with a wavelength of 5.4 m ($\lambda = \frac{v_{min}}{f_{max}}$), Figure 10 shows the wavelet used in the modeling.

Figures 11 and 12 shows common shot gathers (CSG) in the AVO model taken at 2000 m before and after the fluid substitution, respectively. It is possible to note the first arrival both for P and S waves. The top and bottom reflection of our target are visible in the common shot gather after the fluid substitution. The presence of both reflections is not easily distinguished in the CSG before the fluid substitution because of the low impedance constraint of the body, this result will be discussed in the next section.

Since the velocity analysis will be done for P velocities only, the velocity analysis model consists only of P wave information, Figure 20 shows a common shot gather of the velocity analysis model. It is possible to note the P wave first arrival and a series of weak reflection hyperbolas.

Prior to the analysis of the modeling results it is necessary to make a brief processing of the data obtained in this section of the work. This processing and analysis will be presented in the next section.

ANALYSIS

Since there are two different models for two different analysis, the processing and analysis will be split in two parts: an AVO analysis part and a velocity analysis part.

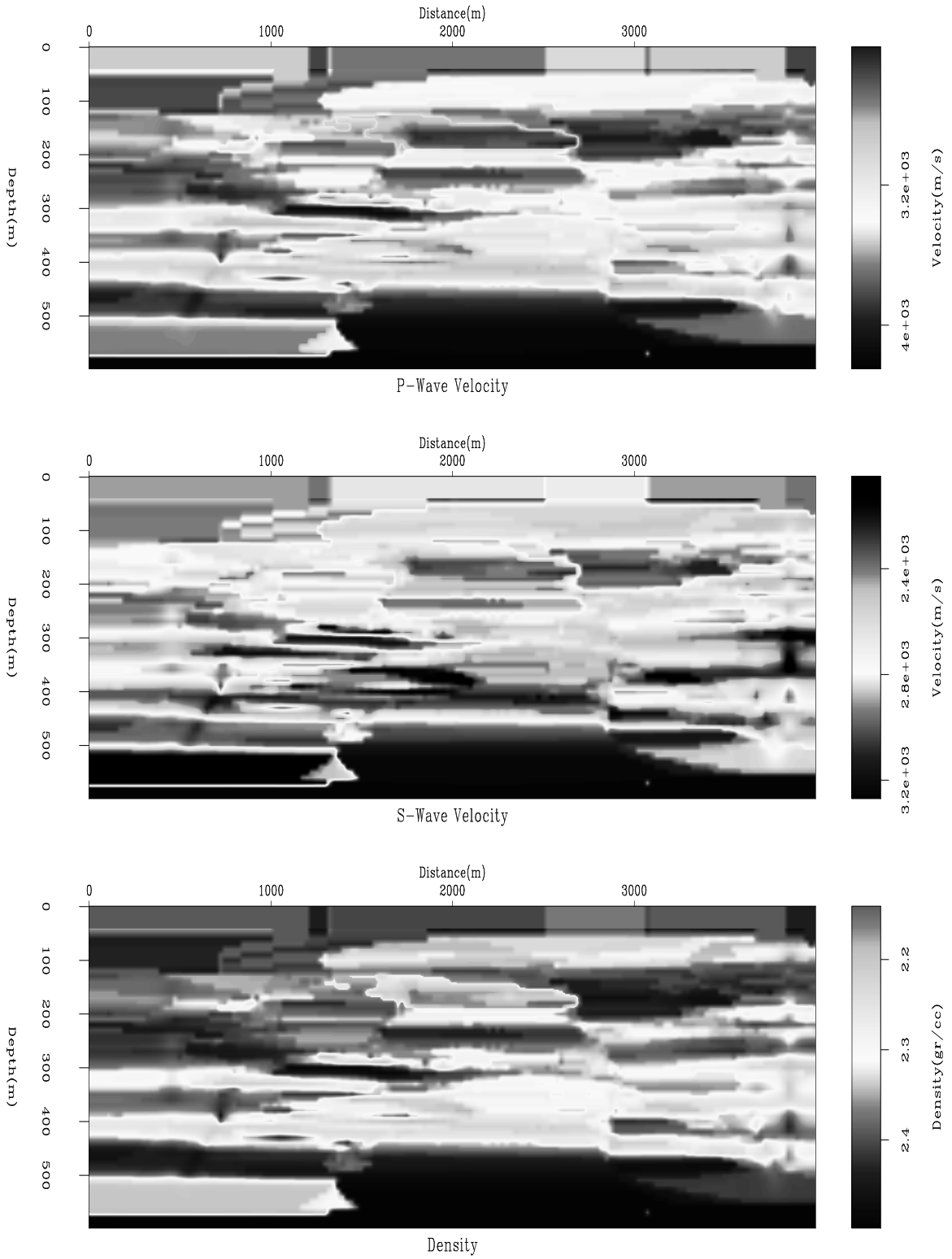


Figure 8: Oil-substituted sections. `daniel1-oil_plot` [ER]

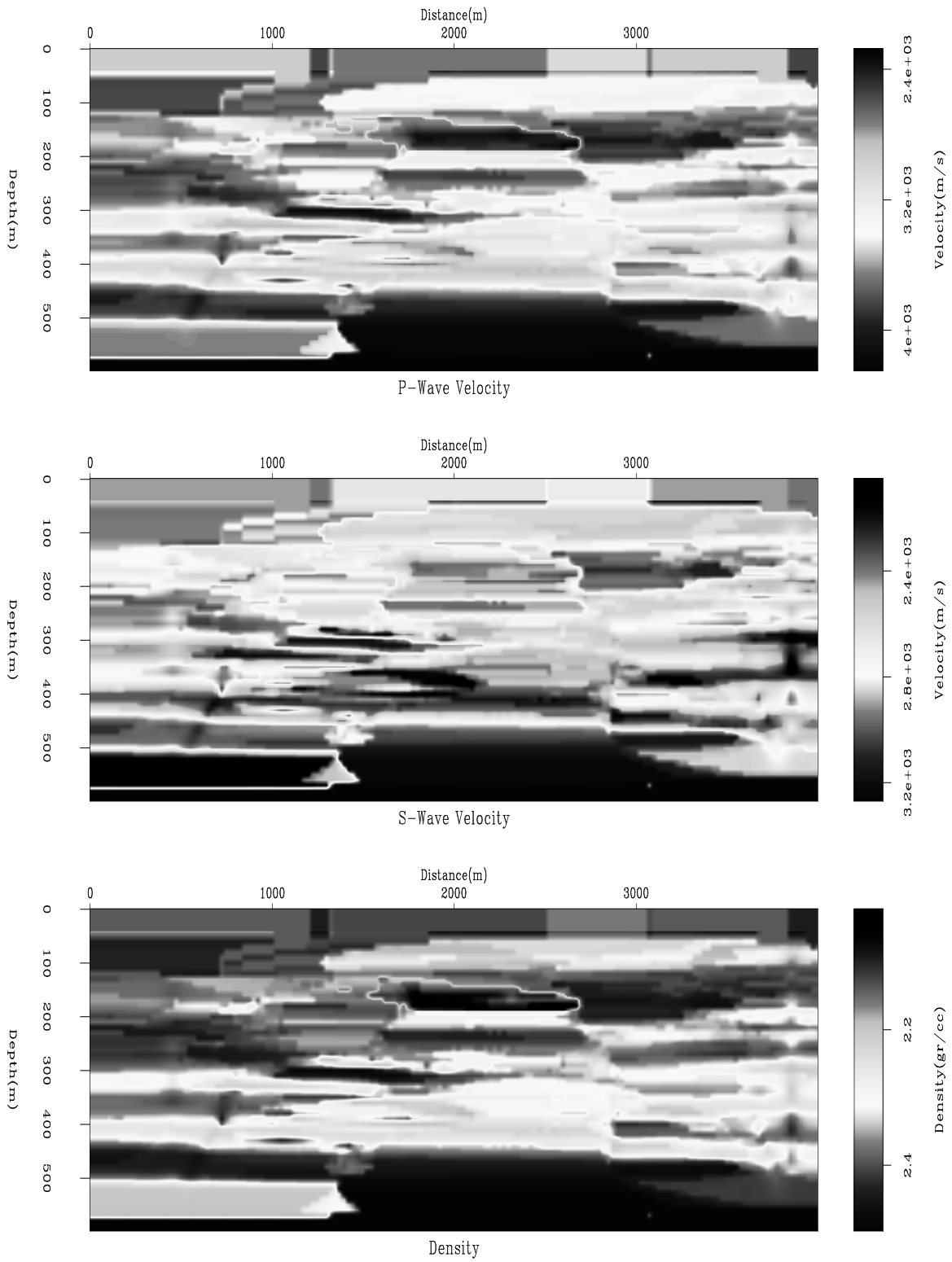


Figure 9: Gas-substituted sections. `daniel1-gas_plot` [ER]

Figure 10: Ricker wavelet used for the modeling. `daniel1-Wav` [ER]

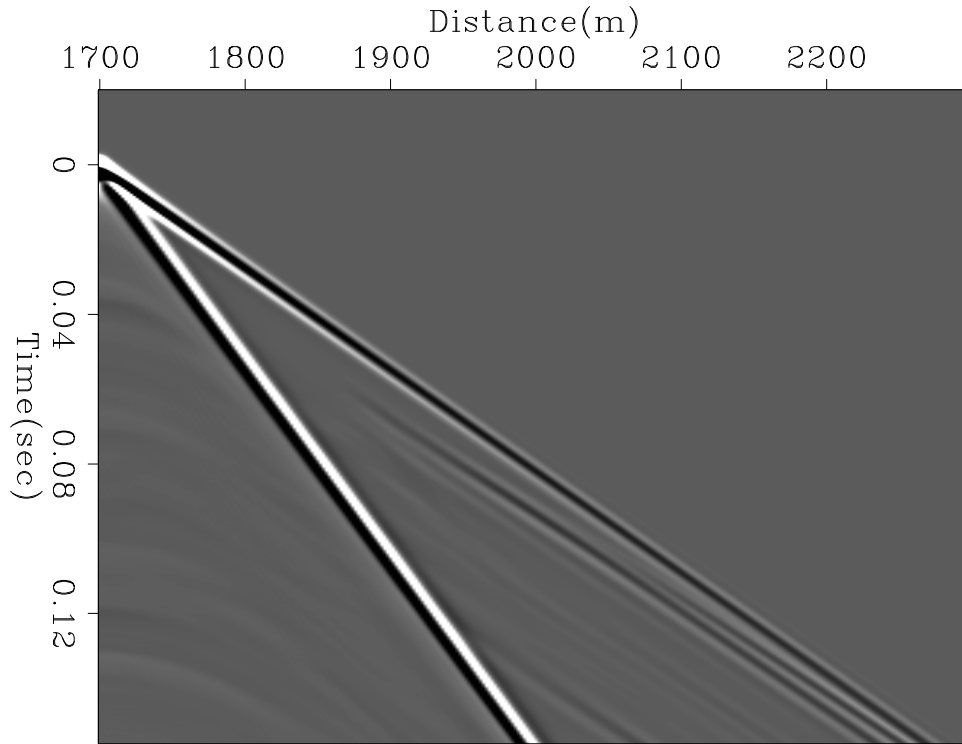
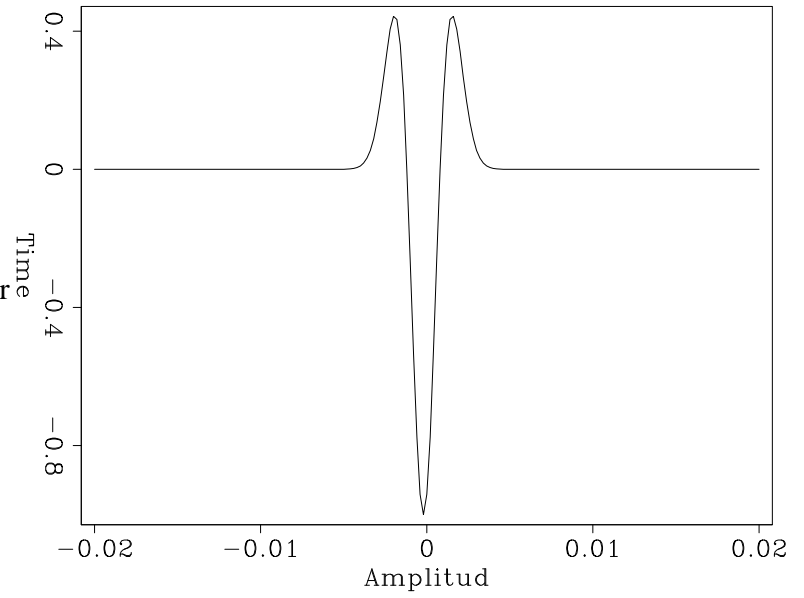


Figure 11: Common shot gather taken in the center of the model. `daniel1-center` [ER]

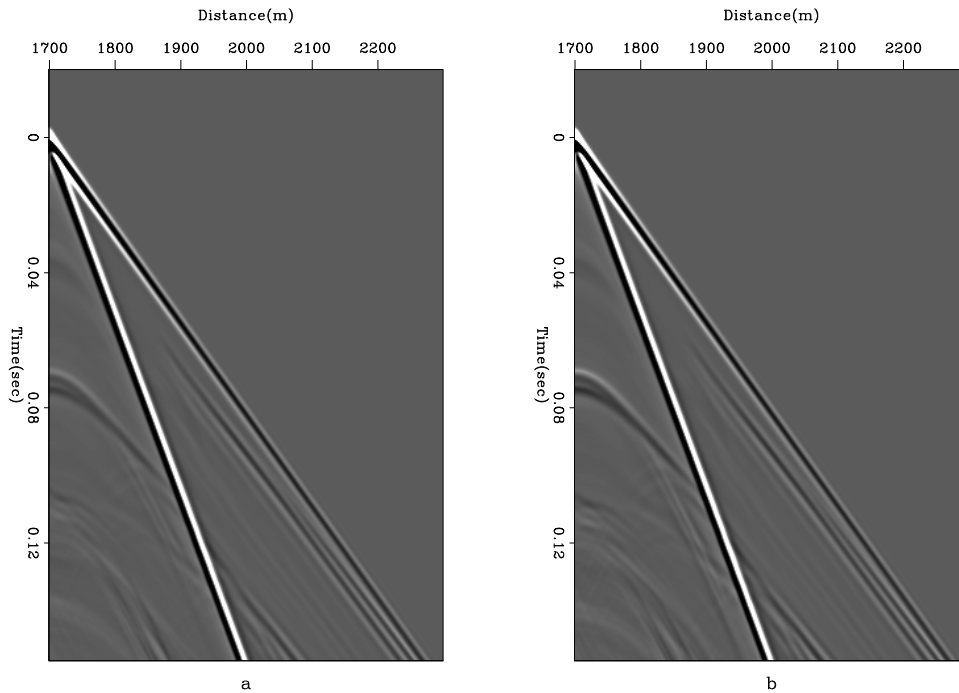


Figure 12: Common shot gathers taken in the center of the model after the fluid substitution. **a** brine→oil substitution. **b** brine→gas substitution. daniel1-center_og [ER]

AVO analysis

The first step in the analysis was to further process the raw data by doing a simple CMP sort. Ideally, the receiver spacing in a survey (ΔG) should be twice the shot spacing (ΔS). However, the geometry which constrained our modeling ($\Delta S = \Delta G$) provides for some headaches in the sorting process (Claerbout and Black, 1997). The CMP sorting was based on if the offsets were odd or even. Even offsets went to even CMP numbers and odd offsets went to odd CMPs. The end result was twice the CMP sampling with half the traces in each CMP as were in the shot gathers. With 60 shots (spanning 120 m) we ended up with 159 CMP locations (spanning 159m). There were 20 CMP locations which were fully sampled, that is all their offsets had trace information. These correspond to the points from 2084m-2104m. This section at zero offset roughly estimates what a stacked section in this part of the model would look like.

Another problem is the direct wave arrivals for both the P-wave and S-wave. In Figure 11 the direct S-wave cuts across the far receiver traces where AVO effects can be important. Also, these high amplitude primary arrivals can inhibit good velocity analysis. Therefore, a simple velocity mute was used for the CMP gathers to better view the data.

It is possible to note in Figure 13, the differences in the P velocity for the sand body selected for the study with the three different fluid properties after the fluid substitution.

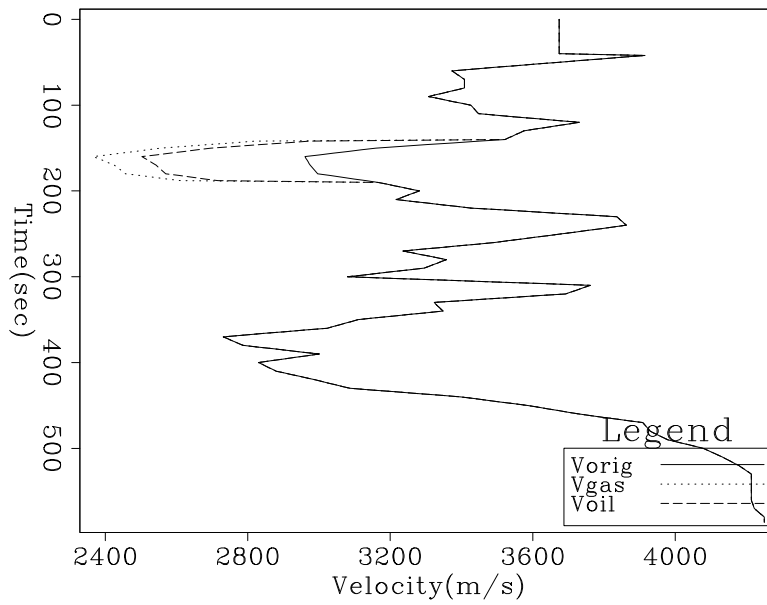


Figure 13: P velocity comparison for the sand body with three different fluids. daniel1-velcomp [ER]

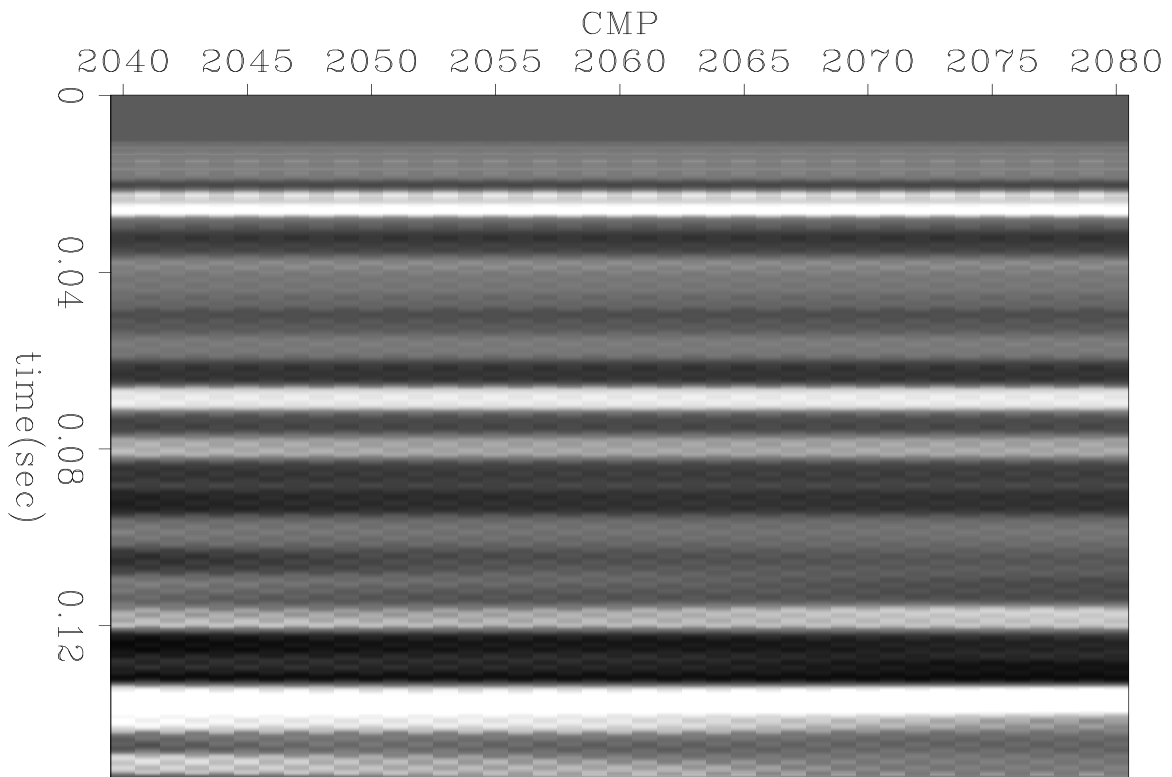


Figure 14: Zero-offset section for brine filled pore space. daniel1-brine_section [CR]

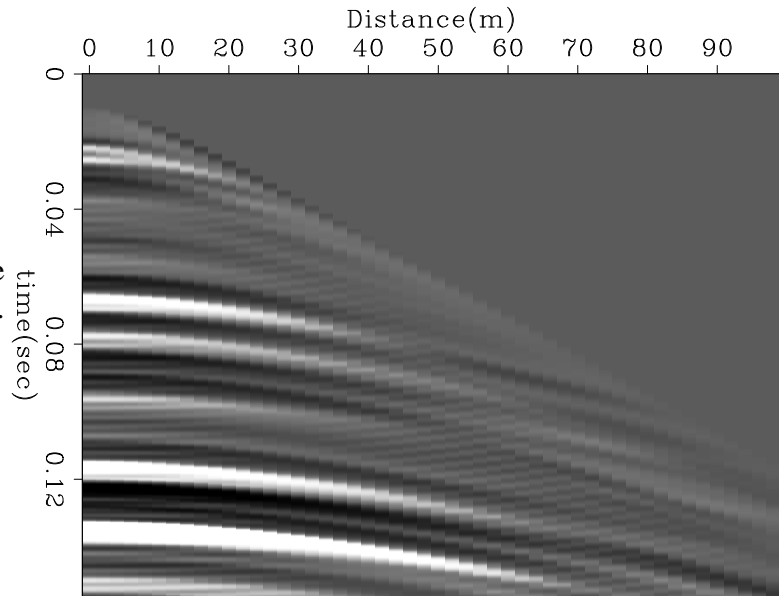


Figure 15: CMP from brine section at midpoint 2100m. `daniel1-brine_cmp` [CR]

Brine Saturated Pore Space

The section created from the original brine-saturated model is shown in Figure 14. The first thing to notice is that the amplitudes for the reflections are not very strong. This is because the impedance contrast between the two is not enough to generate a strong reflection. The reflection present does exhibit the 180° phase change which is expected from a wave reflecting off a layer with lower impedance (Sheriff and Geldart, 1995). The reflection from the bottom of the body is also present. This reflection does not show the 180° phase change because the lower unit has a relatively high impedance. The offset in the brine gathers, Figure 15, does not show any particular change with offset, except that the expected decrease in amplitude with offset is observed. An equation which relates P-wave reflection amplitude with increasing angle (or offset) is Shuey's approximation:

$$R(\Theta) \approx R_0 + \left[ER_0 + \frac{\Delta v}{(1-\nu)^2} \right] \sin^2 \Theta + \frac{\Delta V_p}{V_p} [\tan^2 \Theta - \sin^2 \Theta] \quad (9)$$

where ν is Poisson's ratio, R_0 is the normal incidence reflection coefficient, and E is a term involving the velocity and density changes (Mavko, 2000). Basically this equation, and other AVO equations, show that with little change in Poisson's ratio over a contact, the amplitude should decrease with offset, which is observed in the Figure 15.

Oil Saturated Pore Space

This is the section produced by using the Gassman's relations to substitute oil for brine. The big difference is the fact that the interfaces at the top and bottom of our sand are very distinguishable. The reason is that the impedance contrast is much greater because the P-wave velocity decreases with the substitution of oil since the Bulk modulus of oil is about 1/4 that

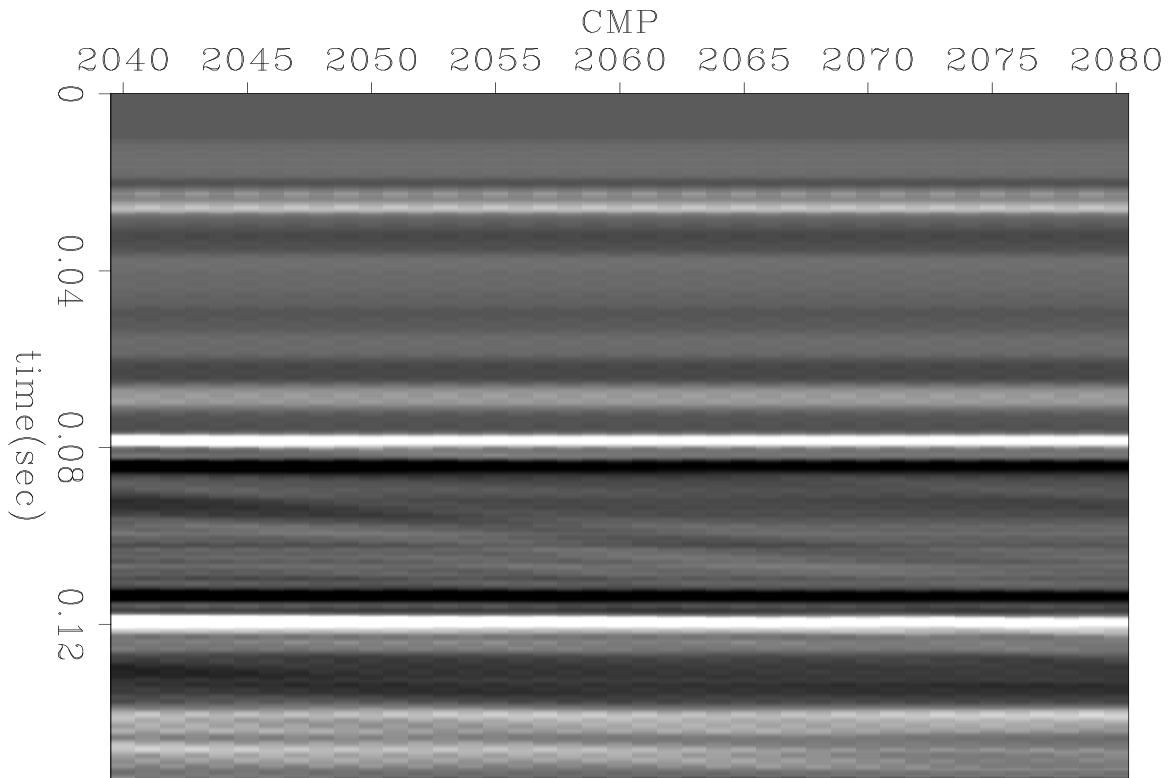


Figure 16: Zero-offset section for oil filled pore space. `daniel1-oil_section` [CR]

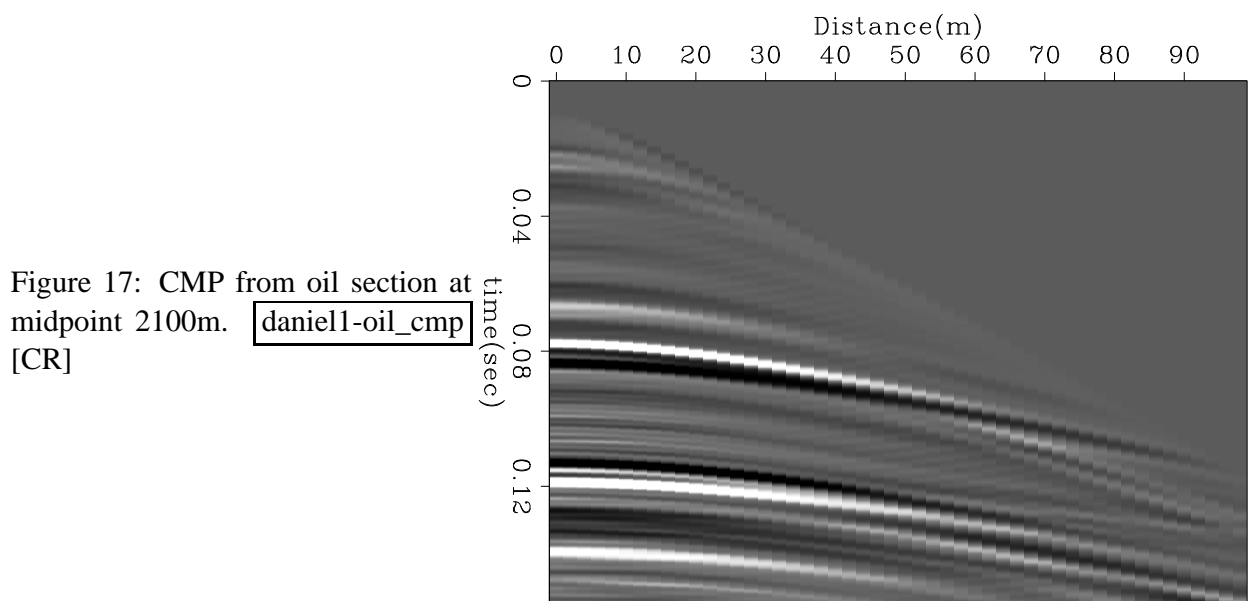


Figure 17: CMP from oil section at midpoint 2100m. `daniel1-oil_cmp` [CR]

of brine. Figure 16 shows the section. It is clear that the data does not change above the sand body, but at the contact and later, the arrivals are changed. Figure 17 shows the CMP gather from the midpoint at 2100 meters. There is good indication of a shear-wave arrival on the CMP gather for both the top and bottom reflection. Also, there is what appears to be a head-wave arrival from a refraction at the base of our sand.

The greater offsets for the oil section have much higher amplitude than for the brine section, however there is not an appreciable increase in AVO which is often expected with hydrocarbon indication (Mavko and Mukerji, 1998). Referring to equation (9), there still is not enough of a change in Poisson's ratio to yield an increase in amplitude with offset. Rather, the amplitude stays about the same magnitude, or decreases a little with increasing offset.

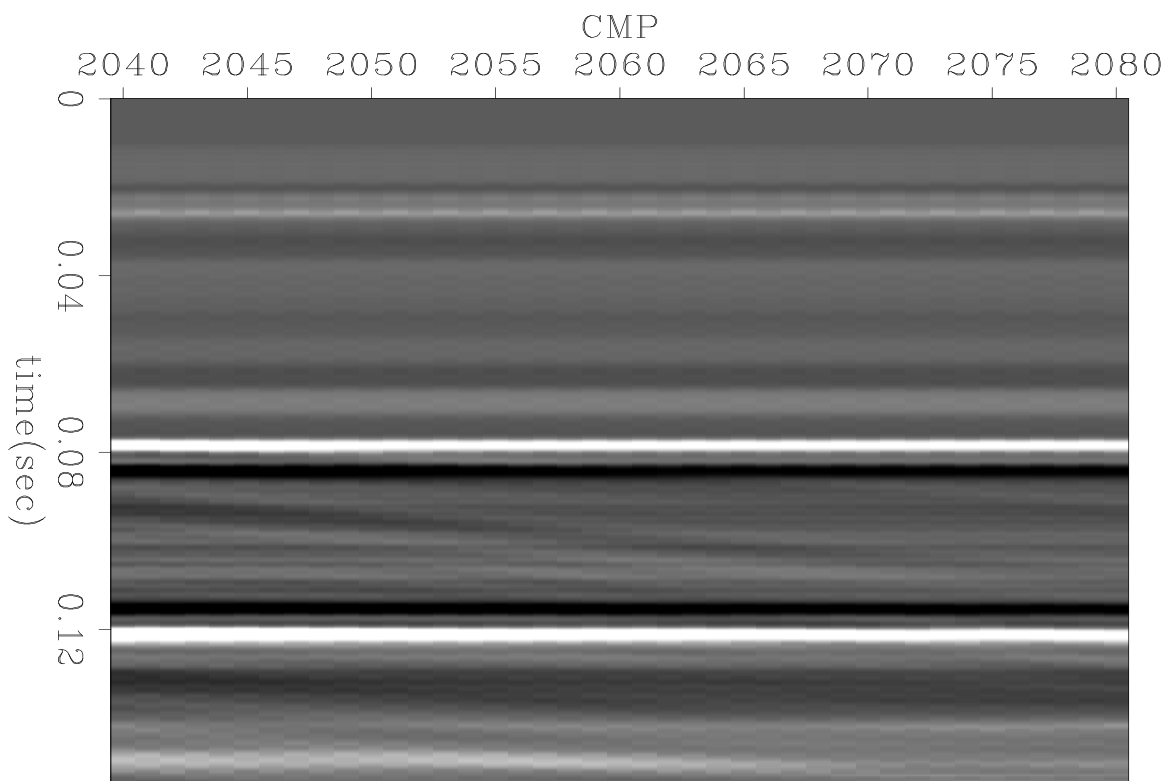
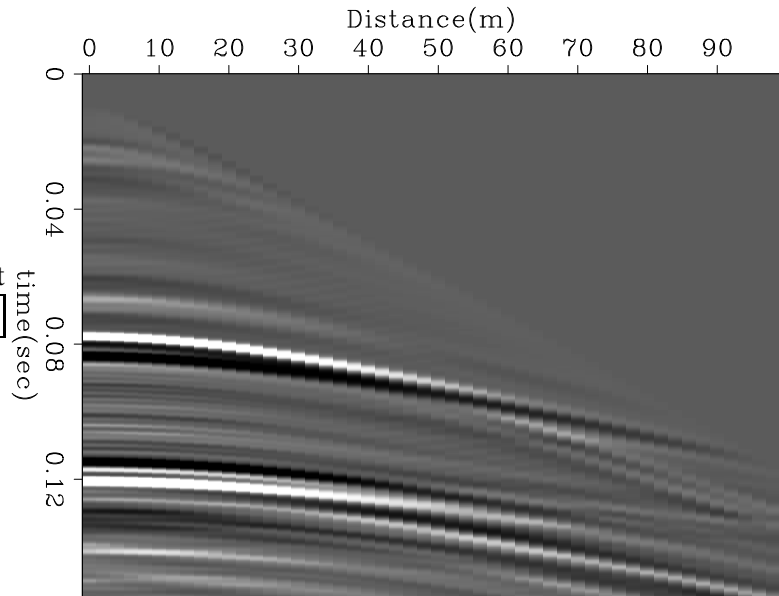


Figure 18: Zero-offset section for gas filled pore space. daniel1-gas_section [CR]

Gas Saturated Pore Space

The final fluid substitution was that of brine for gas. The gas is both the less dense and least rigid of all the fluids used, and thus the impedance contrast between our sand body and the shale units around the body was the greatest in this model. Figure 18 shows the last section. The amplitudes are the the highest for this fluid substitution because the reflection coefficient is the largest. Like in the oil section, many interesting effects of using elastic modeling can be seen, including *S*-wave reflections and what appear to be *S*-wave refractions.

Figure 19: CMP from gas section at midpoint 2100m. `daniell-gas_cmp` [CR]



AVO theory, according to equation (9), predicts that for a negative reflection coefficient and a decrease in Poisson's ratio, as in a gas sand below a shale, the amplitude will increase with offset (Ostrander, 1984). In fact, this is what was noted in the gas saturated model. The CMP in Figure 19 clearly shows that when gas is the constituent of the pore space, amplitude will increase with offset. Also, when there is a positive reflection coefficient, and increase in Poisson's ratio, as in a gas sand overlying a shale, the amplitude will also increase with offset. This is what we see in the bottom reflector. Thus when the sand body is gas saturated, the AVO effect causes increase in amplitude with offset at both interfaces.

Velocity Analysis

The *velocity modeling* result was used in this part of the paper. The common shot gathers were processed in order to obtain the CMP gather corresponding to the exact well position for the velocity analysis.

The processing consisted of basic steps, first of all a CMP sorting was executed on the common shot gathers. A prediction error filter was calculated on each CMP gather in order to proceed with deconvolution. This basic processing sequence was followed with a bandpass filtering and an AGC (Claerbout, 1999).

Figures 20 and 21 shows a common shot gather and a common midpoint gather after the sequence processing, respectively, it is possible to note that after the sequence processing applied to the data set the reflection hyperbolas are very well defined, and the common midpoint gather has a behavior of a sequence of layers without structure component or strong lateral velocity variations.

The velocity analysis was performed on the CMP gather showed in Figure 21; the result is showed in Figure 22 with the picking result superimposed. A comparison between the seismic

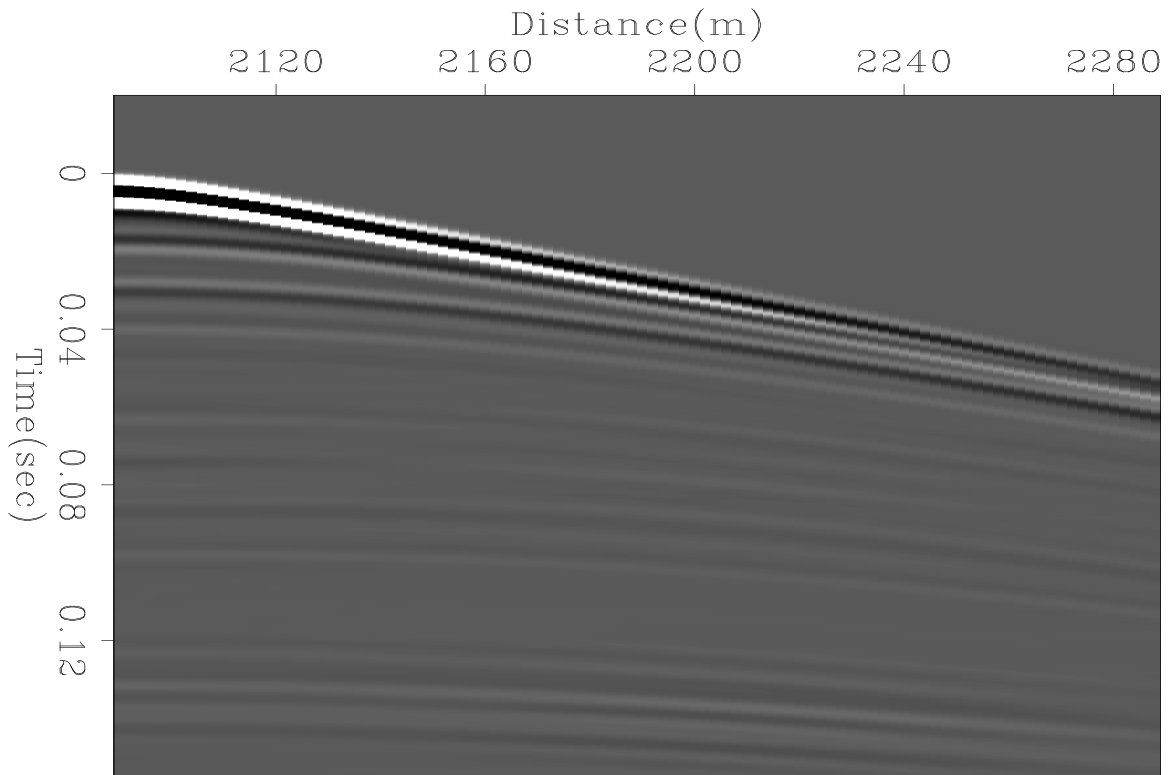


Figure 20: Common Shot Gather from velocity analysis modeling. daniel1-csg [CR]

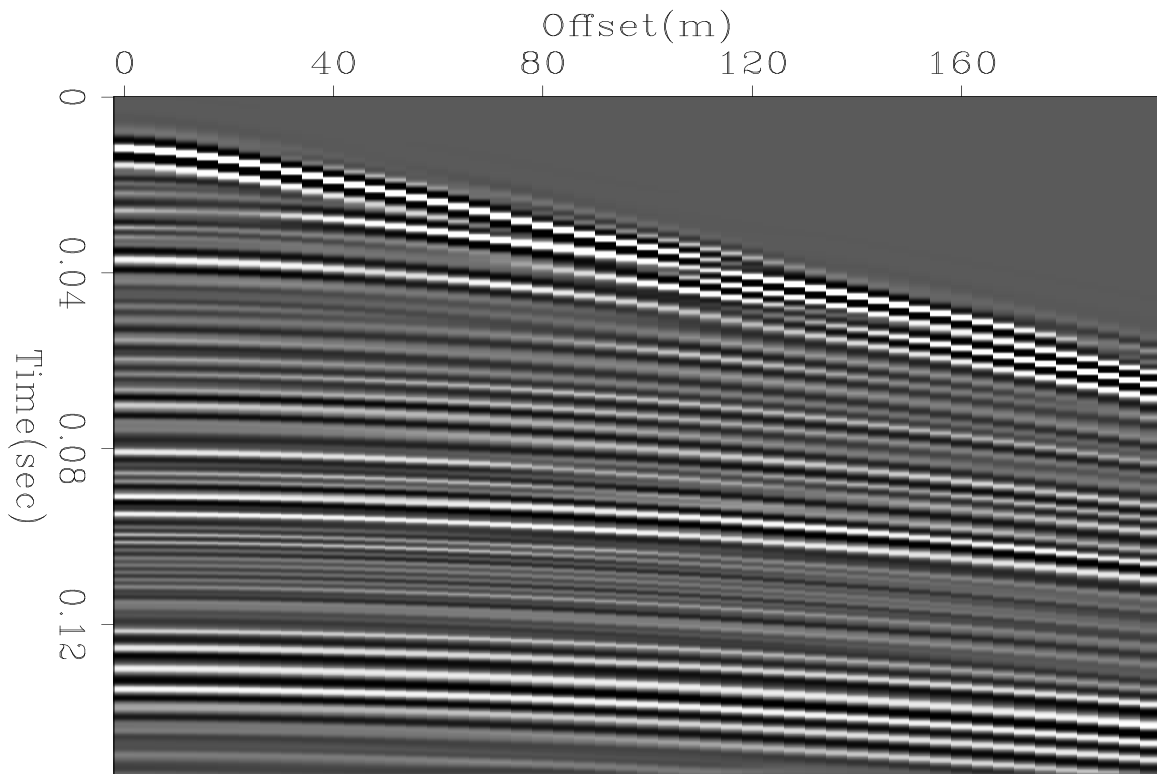


Figure 21: Common Midpoint Gather corresponding to the well position. daniel1-cmp [CR]

rms velocity and the “well *rms*” velocity, obtained by converting the well velocity into *rms* velocity in time, is showed in Figure 23. It is possible to note that seismic velocities follow the same tendency as the well velocity. The difference between those velocities are caused by the difference between the seismic experiment and well experiment.

The seismic experiment reads velocities with an horizontal component while the well experiment reads velocities with a vertical component only. This difference produces difference in the values of the velocities that both experiments read.

Another source of differences is the dissimilarity in the frequency content of both experiments. Interval velocity conversion was performed on this actual seismic *rms* velocity, the

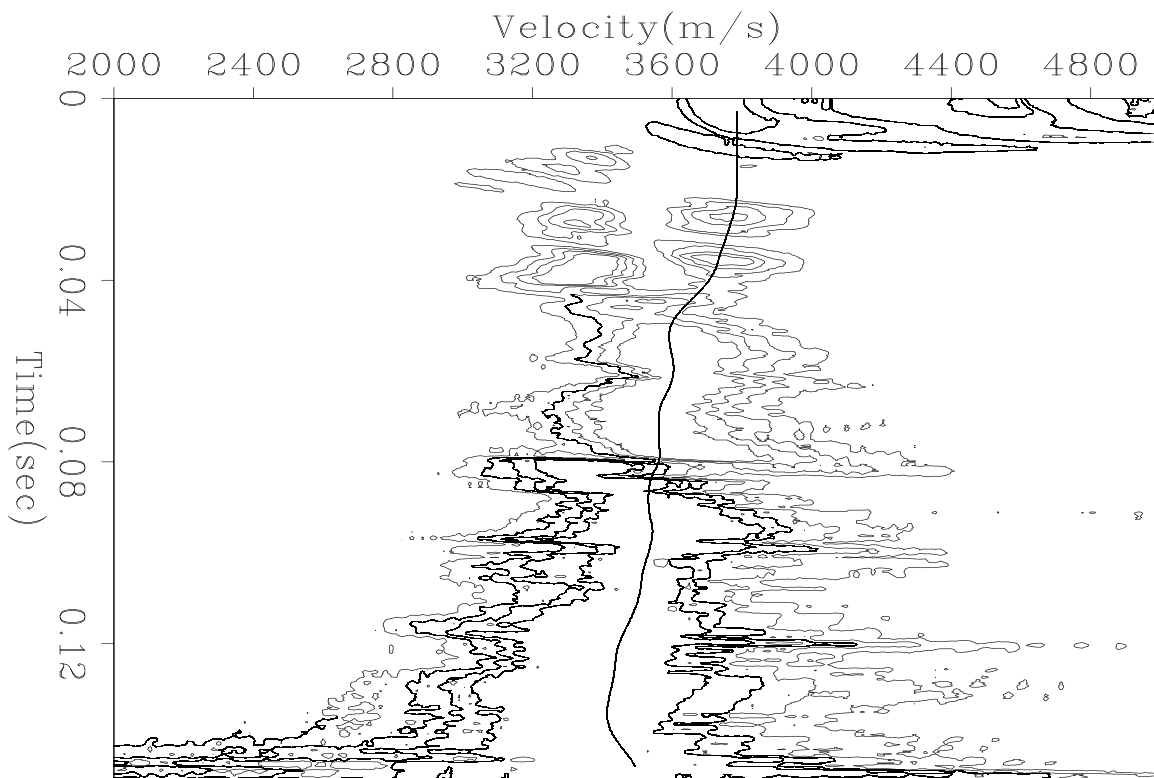


Figure 22: Velocity analysis for CMP gather in Figure 21. [daniel1-velan](#) [CR]

methodology discussed in (Clapp et al., 1998; Rosales, 2000) for interval velocity conversion was used in order to obtain the interval velocity for this CMP. The comparison between the well velocity and the seismic interval velocity is presented in Figure 24.

It is possible to note the frequency difference between both velocities. Seismic velocities have a lower frequency content than well velocities. This difference is mainly originated by the wavelet used for the modeling.

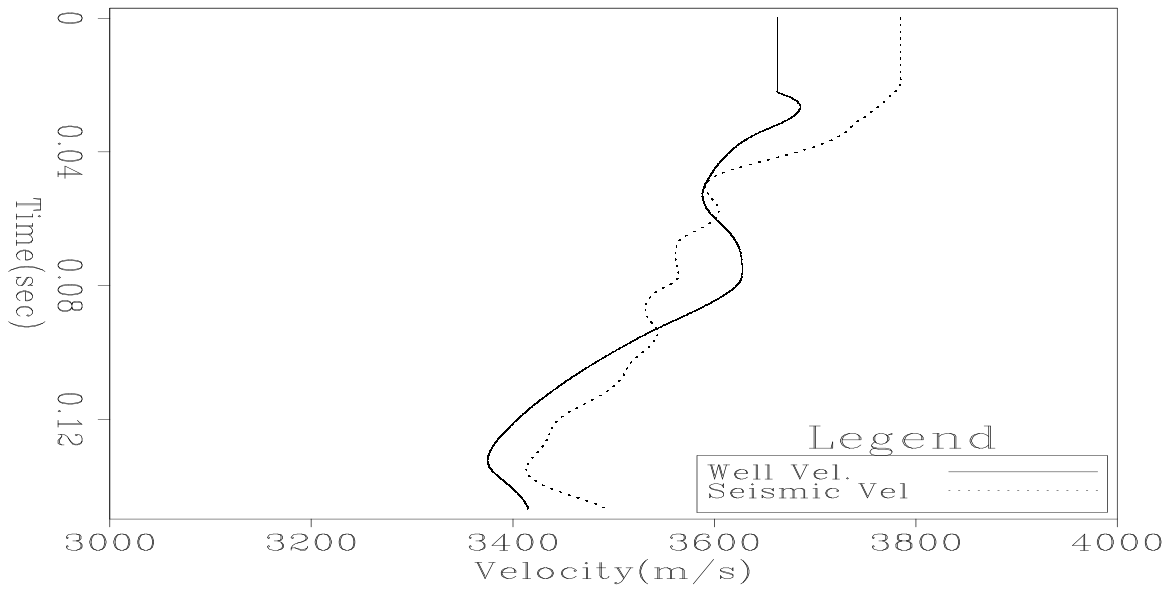


Figure 23: RMS velocity comparison for well velocity and seismic velocity. daniel1-rmsvelcomp [CR]

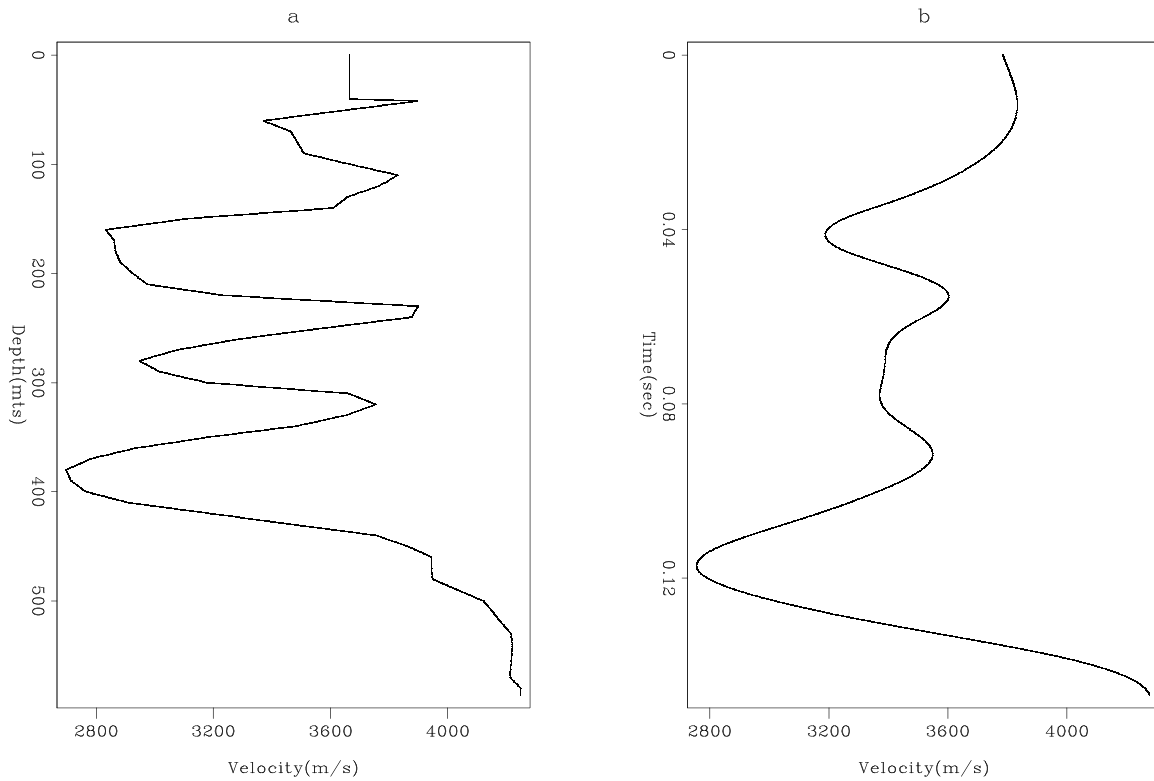


Figure 24: Interval velocity comparison for well velocity and seismic velocity. daniel1-intvelcomp [CR]

CONCLUSION

The analysis of seismic response based on well interpolated data was done. Our results follow the AVO theory based on Shuey's relation, equation (9), for amplitude variations with offset.

The interpolated data obtained from the given well data follows a geological distribution characteristic of a depositional system. It is also possible to note that the interpolation result correlate very well with the original well information. These results correlate with the original data distribution.

Fluid substitution with *Gassmann's equations* brings changes in the velocity model; we observe that the P velocity decreases with changes in the fluid type and that the lowest velocity in the sand body selected for the study corresponds to the gas substitution (Figure 13). It was also noted that there was a contrary behavior for the S velocity, since the shear modulus remains the same in the fluid substitution recipe, the S velocity increment observed is due to the density decrease after the fluid substitution.

A high frequency seismic modeling with different velocity models brought different seismic responses. These different responses were due only to differences in the rock fluids. These behaviors reinforce the fact that different fluid type in the rock yield different seismic responses, especially in the amplitude behavior.

The fact that the highest amplitude was the one with gas saturated sand confirms the *bright spot* phenomena observed in real seismic data in the presence of gas. This observation is an important in real life productions in order to predict gas reservoirs in the subsurface with seismic data.

The velocity analysis corroborates the frequency dependence of the velocity, since it was possible to note that seismic velocities are smoother than well velocities, but both velocities follow the same tendency.

Seismic velocities are different to well velocities not only in the frequency content but also in the velocity values. This value difference is probably due to the different components of the velocity that both experiments measure.

APPENDIXES

AVO - Shuey's Approximation

From Mavko (2000) we have, P-wave reflectivity versus angle:

$$R(\theta) \approx R_0 + [E R_0 + \frac{\Delta v}{(1-v)^2}] \sin^2 \theta + \frac{1}{2} \frac{\Delta V_p}{V_p} [\tan^2 \theta - \sin^2 \theta] \quad (10)$$

$$R_0 \approx \frac{1}{2} \left(\frac{\Delta V_p}{V_p} + \frac{\Delta \rho}{\rho} \right) \quad (11)$$

$$E = F - 2(1 + F) \frac{1 - 2\nu}{1 - \nu} \quad (12)$$

$$F = \frac{\frac{\Delta V_p}{V_p}}{\frac{\Delta V_p}{V_p} + \frac{\Delta \rho}{\rho}} \quad (13)$$

Empirical relations for estimating V_s from V_p (Mavko, 2000)

Lithology	a_i2	a_i1	a_i0
Sandstone	0	0.80416	-0.85588
Limestone	-0.05508	1.01677	-1.03049
Dolomite	0	0.58321	-0.07775
Shale	0	0.76969	-0.86735

Castagna et al. (1992) relation used in this work is

$$V_s = a_{i2} V_p^2 + a_{i1} V_p + a_{i0} \quad (14)$$

Parameters files

This is the parameter file for the Kriging program

```

Parameters for KT3D
*****

START OF PARAMETERS:
./all.dat          \file with data
1  2  3  9  0      \ columns for X, Y, Z, var, sec var
-1.0e21  1.0e21    \ trimming limits
0                 \option: 0=grid, 1=cross, 2=jackknife
xvk.dat           \file with jackknife data
1  2  3  9  0      \ columns for X,Y,Z,vr and sec var
1                 \debugging level: 0,1,2,3
kt3d.dbg          \file for debugging output
velocity.out      \file for kriged output
40 -1000.0  50.0  \nx,xmn,xsiz
160  0.0  25.0    \ny,ymn,ysiz
60  -600.0  10.0  \nz,zmn,zsiz
1  1  1           \x,y and z block discretization
0  10            \min, max data for kriging
0               \max per octant (0-> not used)
1500.0 3000.0 50.0 \maximum search radii
0.0  0.0  0.0    \angles for search ellipsoid
1  2655.32       \0=SK,1=OK,2=non-st SK,3=exdrift
0 0 0 0 0 0 0 0  \drift: x,y,z,xx,yy,zz,xy,xz,zy
0               \0, variable; 1, estimate trend
extdrift.dat     \gridded file with drift/mean
4               \ column number in gridded file
1  0.15         \nst, nugget effect

```



```

2      1.0  0.0  0.0  0.0      \it,cc,ang1,ang2,ang3
      87.434 87.434 50      \a_hmax, a_hmin, a_vert

```

This is the parameter file for the Variogram calculation

```

Parameters for GAMV
*****

```

```

START OF PARAMETERS:
./all.dat          \file with data
1  2  3            \  columns for X, Y, Z coordinates
1  9              \  number of variables,column numbers
-1.0e21  1.0e21   \  trimming limits
gamv_v3.out       \file for variogram output
9                \number of lags
50.0             \lag separation distance
30.0             \lag tolerance
2               \number of directions
0.0  90.0 50.0   0.0  90.0  50.0 \azm,atol,bandh,dip,dtol,bandv
0.0  90.0 50.0   90.0  90.0  50.0 \azm,atol,bandh,dip,dtol,bandv
1              \standardize sills? (0=no, 1=yes)
1              \number of variograms
1  1  1        \tail var., head var., variogram type

```

REFERENCES

- Chen, Q., and Sidney, S., 1997, Seismic attribute technology for reservoir forecasting and monitoring: *The Leading Edge*, **16 no.5**, 445–450.
- Claerbout, J. F., and Black, J. L., 1997, Basic earth imaging: Class notes, http://sepwww.stanford.edu/sep/prof/bei/toc_html/index.html.
- Claerbout, J., 1999, Geophysical estimation by example: Environmental soundings image enhancement: Stanford Exploration Project, <http://sepwww.stanford.edu/sep/prof/>.
- Clapp, R. G., Sava, P., and Claerbout, J. F., 1998, Interval velocity estimation with a null-space: *SEP-97*, 147–156.
- Deutsch, C. V., and Journel, A. G., 1998, *Gslib geostatistical software library and users guide*: Oxford University Press.
- Journel, A. G., 2000, *Geostatistics for spatial phenomena : Course reader*: Stanford University.
- Mavko, G., and Mukerji, T., 1995, Fluid substitution; estimating change in vp without knowing vs: *Geophysics*, **60**, no. 06, 1750–1755.
- Mavko, G., and Mukerji, T., 1998, A rock physics strategy for quantifying uncertainty in common hydrocarbon indicators: *Geophysics*, **63**, no. 06, 1997–2000.

Mavko, G., 2000, GP262 Rock Physics Spring 2000 : Course reader: Stanford University.

Ostrander, W. J., 1984, Plane-wave reflection coefficients for gas sands at nonnormal angles of incidence: *Geophysics*, **49**, no. 10, 1637–1648.

Rosales, D. A., 2000, Research interest: Improving the velocity model: *SEP-103*, 69–78.

Sheriff, R., and Geldart, L., 1995, *Exploration seismology*: Cambridge.

White, R., 1998, Well tie, fluid substitution and avo modeling; a north sea example: *Geophysical Prospecting*, **64**, no. 03, 323–346.

Yilmaz, O., 1987, *Seismic data processing*: Soc. Expl. Geophys.

